



Source parameters and triggering links of the earthquake sequence in central Italy from 2009 to 2016 analyzed with GPS and InSAR data

Leyang Wang^{a,c,d}, Hua Gao^{a,c,*}, Guangcai Feng^b, Wenbin Xu^e

^a Faculty of Geomatics, East China University of Technology, Nanchang 330013, China

^b School of Geoscience and Info-Physics, Central South University, Changsha 410083, China

^c Key Laboratory of Watershed Ecology and Geographical Environment Monitoring, NASG, Nanchang 330013, China

^d Key Laboratory for Digital Land and Resources of Jiangxi Province, Nanchang 330013, China

^e Department of Land Surveying and Geo-informatics, The Hong Kong Polytechnic University, Hung Hom, Kowloon, Hong Kong, China

ARTICLE INFO

Keywords:

2016 Central Italy earthquakes

Focal parameters inversion by InSAR and GPS data

Coulomb stress change and triggering relation

ABSTRACT

From 2009 to 2016, four earthquakes ($M_w > 6$) occurred in central Italy, which are the Apr. 6th, 2009 earthquake, Aug. 24th, 2016 earthquake, Oct. 26th, 2016 earthquake and Oct. 30th, 2016 earthquake. To investigate their seismic mechanism, triggering relationships and impacts on the surrounding areas, we obtained their coseismic deformation fields using the data of interferometric synthetic aperture radar (InSAR) and global positioning system (GPS). We constructed three variable-strike fault models for the four events which can be more consistent with the actual fault and improve the overall fitting precision. On this basis, we calculated the coseismic slips of the first two earthquakes respectively and obtained that of the last two earthquakes by a joint inversion method. Then the Coulomb stress changes of those four earthquakes were calculated. The results show that these earthquakes are mainly caused by normal faults that strike approximately NW-SE or NNW-SSE and dips to SW or WSW with angles between 33° and 47°. All these events are shallow earthquakes, and the main fault slips are located in the area with depth of 0–10 km, accompanied by some surface ruptures. The maximal slip with a value of 3.44 m at ~4 km depth was caused by the Oct. 30th, 2016 earthquake. The inverted magnitudes of the four earthquakes are M_w 6.26, M_w 6.20, M_w 6.19 and M_w 6.60. The stress changes indicate that the former earthquake accelerated the latter one successively. Moreover, there is a seismic gap between the regions of the Apr. 6th, 2009 and Aug. 24th, 2016 earthquakes and a high stress-accumulating area in the south of the Apr. 6th, 2009 earthquake region. So, the Montereale fault in the gap and the Barisciano fault located on the southeast of the Paganica fault might have great earthquake risks due to the massive accumulated stress.

1. Introduction

The complex tectonic environment in central Italy is governed by the interaction between the Eurasian plate and the Adriatic plate under the Adriatic Sea. The Adriatic plate is subducting westward beneath the Apennines Peninsula, and the central Apennines Peninsula is extending in a north-east to south-west direction at a rate of 3 mm/yr (Hunstad et al., 2003; D'Agostino et al., 2009; Faure et al., 2010). This extension is accommodated on a series of active normal faults and normal mechanism earthquakes. Since 1976, dozens of earthquakes ($M_w > 5.0$) that occurred in the Apennine Peninsula and most of them occurred in the mountains of central Italy. Most earthquakes ($M > 6.0$) were caused by normal faults, such as the 1997 Umbria-Marche M_w 6.0 event, 2009 L'Aquila M_w 6.3 event and the three $M_w > 6.0$ earthquakes in 2016 (USGS, 2018) (Fig. 1).

Earthquake source parameters are important in earthquake studies. The 2009 L'Aquila earthquake (hereafter referred to as Event A) was caused by the Paganica fault on the northeast of the Paganica town, which is a normal fault, striking NW-SE and dipping ~50° (Walters et al., 2009; Cirella et al., 2009). The three earthquakes occurred in 2016 (hereafter referred to as Events B/C/D) all strike NNW-SSE and dipped SW (USGS, 2018; GCMT, 2018; INGV, 2018). Studies on Events A and B using the geodetic observations (GPS and InSAR data) got generally consistent source parameters but different strike and dip angles of Event B (Valensise et al., 2016; Cheloni et al., 2017; Xu et al., 2017). Furthermore, for Event B, different data bring different slip distribution models. The slip distribution model obtained by InSAR is continuous, which coincides with the shape of the coseismic deformation field of InSAR (Huang et al., 2017; Xu et al., 2017). However, the results obtained by GPS and seismic wave are dispersed (Magnoni and

* Corresponding author at: Faculty of Geomatics, East China University of Technology, Nanchang 330013, China.

E-mail address: gaoahuastudent@163.com (H. Gao).

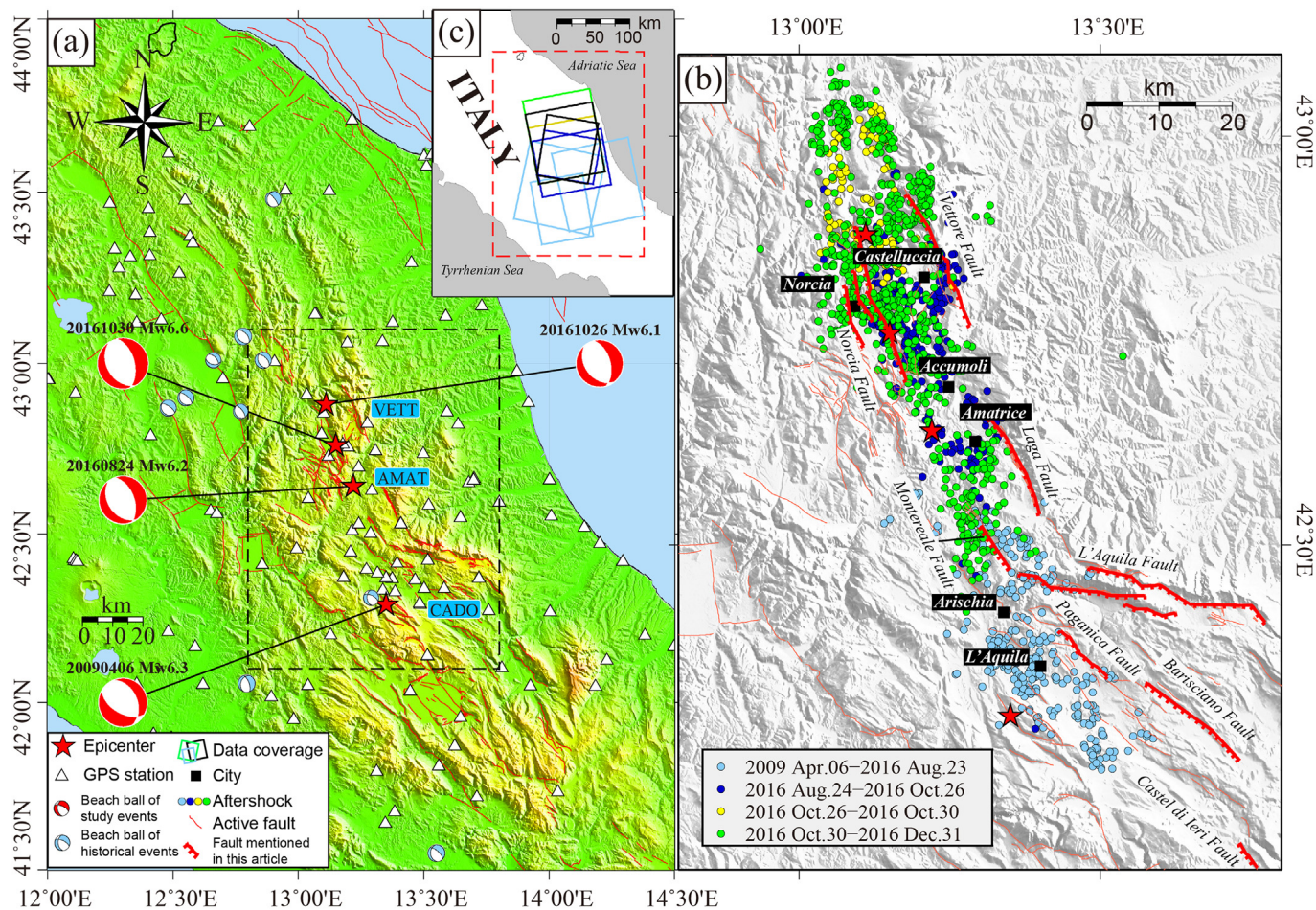


Fig. 1. (a) Tectonic setting of the study area and historical earthquakes. The red stars indicate the epicenters of the four earthquakes. The red lines are active faults in the study area. The blue and white beach balls are the historical earthquakes from 1976 to 2009 ($M_w > 5.0$; data from GCMT (2018)). (b) Aftershocks and active faults in the study area. The red stars indicate the epicenters of the four earthquakes. The red lines are active faults, and the bold red lines are the main faults that will be discussed later. The light blue, blue, yellow and green dots are the aftershocks of the four earthquakes ($M_w > 3$, data from INGV (2018) and UGSG (2018)). (c) SAR data coverage. The light blue, blue, green and black rectangles are the SAR data coverage of Event A, Event B, Event C, Event D and the combined influence of Events C and D, respectively. (For interpretation of the references to colour in this figure legend, the reader is referred to the web version of this article.)

Casarotti, 2016; Tinti et al., 2016). Therefore, it is necessary to further study the source parameters of Event B with both the GPS and InSAR data. Besides, most studies combined Events C and D or separate them using only a pair of ascending images, because the time between the earthquakes was very short (4 days) (Cheloni et al., 2017; Xu et al., 2017). However, doing this leads to the inversion result inaccurate. After Event B, the Coulomb stress increased about 0.1 MPa in the vicinity of Mt. Vettore near the surface (depth < 1 km) (Huang et al., 2017; Mildon et al., 2017). Whether Events C and D were triggered by Events A and B is an interesting question. Mildon et al. (2017) systematically studied the static Coulomb stress changes from Event A to Event D based on the historical earthquakes. Mildon et al. (2017) found that a series of earthquakes occurred in central Italy in 2016 and 2017 (Events B/C/D and four $M_w > 5$ aftershocks occurred in 2017) were caused by the long-term stress loading. However, they used a simplified slip distribution model produced by simple linear slip gradients for Events C and D, so they did not get the accurate stress changes induced by the two earthquakes. Papadopoulos et al. (2017) and Xu et al. (2017) found that there may be a triggering relationship between Events B, C and D based on the P waves and D-InSAR data, respectively. However, there are few studies concerning the impact of these earthquakes on the surrounding areas and the assessment of future earthquake disasters based on geodetic data. The geodetic method can provide more accurate deformation fields, source parameters and slip distribution results

of strong earthquakes. So using geodetic survey can make a systematic study of the four earthquakes and their impact on the surrounding areas. It is of great significance to the long-term earthquake prediction in this area.

In this study, we obtained the coseismic deformation fields of Events A–D using InSAR and GPS data. Then we systematically studied the source parameters of the four earthquakes using InSAR, GPS and field work data. Based on three variable-strike fault models, we calculated, sequentially and synthetically, the stress changes caused by Events A–D. Finally, the triggering relation between these four earthquakes and potential earthquake disasters of the surrounding areas are discussed.

2. Data processing and source parameters inversion

2.1. Data processing

We obtained InSAR data of the four earthquakes from ENVISAT, ALOS, and Sentinel-1A/B satellites (Fig. 1 and Table S1). In this study, the GAMMA software was used to process the InSAR data (Wegmüller and Werner, 1997) and the polynomial fitting method was used to remove phase ramps (Feng et al., 2015b). The line of sight (LOS) deformation fields were obtained after geocoding (Fig. S1). Because of the phase decorrelation caused by large surface ruptures, the SAR pixel offset tracking method (SPO) was selected to map the near-field offset

Table 1

The D-InSAR, SPO and GPS data used in inversion of the four events.

Earthquake	D-InSAR				SPO		GPS station number	
	Descending		Ascending		Ascending			
	N	u (cm)	N	u (cm)	N	u (cm)		
Event A	191	0.79	293(ASAR) + 673(PALSAR)	0.43/0.81	–	–	42	
Event B	555	0.68	591	0.73	–	–	106	
Event C	–	–	814	0.67	–	–	127	
Event D	–	–	1820	0.96	840	48.43	114	
Event C + Event D	1344	1.19	1001	2.42	–	–	–	

Note. N, number of observation points; u, uncertainty.

in Event D (Michel et al., 1999) (Fig. S2). The accuracy of the InSAR deformation fields was assessed by the coseismic GPS data. The GPS and InSAR data were used to jointly inverse the source parameters of the four events.

2.2. Model

We employed the quadtree sampling algorithm to reduce the deformation data of InSAR (Feng et al., 2015a). Then the source parameters were inverted by non-linear inversion and linear inversion. (Feng et al., 2015a; Wang et al., 2017).

Before downsampling, we removed areas with phase decorrelation and significant atmospheric delays. We used accurate incident and azimuth angles to calculate the look vector of each pixel. The numbers of InSAR points and GPS stations used in the model are listed in Table 1. We masked the epicentral region and obtained the uncertainty of the deformation in the far field of the interferograms to measure the accuracy of the deformation field (Table 1), which is used to weight different observations in the inversion. The uncertainty was obtained by Formula 1.

$$u_{\text{field}} = \sqrt{\frac{\sum_{i=1}^n (\text{Fardef}_i)^2}{n - 1}} \quad (1)$$

where u_{field} represents the uncertainty of the deformation field, n represents the number of deformation points, and Fardef_i is the deformation value of point i .

As the basic geometry parameters of Events A, B, C and D (fault location, the length and strike angle) can be determined based on the surface rupture and historical records (Michetti et al., 2000; EMERGE, 2010; Piccardi et al., 2016; Villani et al., 2018; Civico et al., 2018), we directly constructed three variable-strike fault models for the four events and performed linear inversion (Jiang et al., 2013). We chose the width of Events A, B, C and D as large as possible to accommodate the major slip areas of these four events. After several tests, we found that the width of 20 km is suitable. The initial dip angles of the three events are 43°, 52°, 35° and 37° (GCMT, 2018). However, we found that the optimal dip angles of Event A, Event B, Events C and D are 46.8, 44.9°, and 33.5° through iterative inversion. Based on these source parameters, we inverted the fault slip distribution of these four earthquakes. In order to avoid abrupt variations in the slip, the Laplace smoothing was applied between the adjacent fault patches. We used a non-negative least squares algorithm (Feng et al., 2015a,b; Wang et al., 2017) and homogeneous elastic half-space model (Okada, 1985) to solve the slip parameters. For Events A and B, the linear inversion model is as follows (Li, 2016):

$$\begin{bmatrix} \mathbf{d} \\ \mathbf{0} \\ \mathbf{0} \end{bmatrix} = \begin{bmatrix} \mathbf{G}_{ss} & \mathbf{G}_{ds} \\ \lambda \mathbf{H}_{ss} & \mathbf{0} \\ \mathbf{0} & \lambda \mathbf{H}_{ds} \end{bmatrix} \begin{bmatrix} \mathbf{m}_{ss} \\ \mathbf{m}_{ds} \end{bmatrix} + \begin{bmatrix} \varepsilon \\ \mathbf{0} \\ \mathbf{0} \end{bmatrix} \quad (2)$$

$\mathbf{m}_{ss} \geq \mathbf{0}, \mathbf{m}_{ds} \geq \mathbf{0}$

where \mathbf{d} represents the deformation. \mathbf{G}_{ss} and \mathbf{G}_{ds} are the Green function

matrix of strike slip \mathbf{m}_{ss} and dip slip \mathbf{m}_{ds} . \mathbf{H}_{ss} and \mathbf{H}_{ds} are the Laplace smoothing constraint matrices of \mathbf{m}_{ss} and \mathbf{m}_{ds} , respectively. ε is the observation error. λ is the smoothing factor used to balance the observations and the smoothness matrix. Using the method proposed by Jónsson et al. (2002), we selected the smoothing factor for our final solution, as low roughness in significantly worse RMS but higher roughness ratio does not lower the RMS much (the point represented by the green mark in Fig. S3). The shear modulus and Poisson factor were been set as 32 GPa and 0.25.

Because the interval between Events C and D is only four days, most InSAR observations cannot distinguish them, except for one pair of ascending data (Table 1). Therefore, the joint inversion model for Events C and D is as follows:

$$\begin{cases} \begin{bmatrix} \mathbf{d}_a \\ \mathbf{d}_b \\ \mathbf{d}_c \\ \mathbf{0} \\ \mathbf{0} \end{bmatrix} = \begin{bmatrix} \mathbf{G}_{ss1} & \mathbf{G}_{ds1} & \mathbf{0} & \mathbf{0} \\ \mathbf{0} & \mathbf{0} & \mathbf{G}_{ss2} & \mathbf{G}_{ds2} \\ \mathbf{G}_{ss1} & \mathbf{G}_{ds1} & \mathbf{G}_{ss2} & \mathbf{G}_{ds2} \\ \mathbf{0} & \lambda \mathbf{H}_{ss1} & \mathbf{0} & \lambda \mathbf{H}_{ss2} \\ \mathbf{0} & \lambda \mathbf{H}_{ds1} & \mathbf{0} & \lambda \mathbf{H}_{ds2} \end{bmatrix} \begin{bmatrix} \mathbf{m}_{ss1} \\ \mathbf{m}_{ds1} \\ \mathbf{m}_{ss2} \\ \mathbf{m}_{ds2} \end{bmatrix} + \begin{bmatrix} \varepsilon_a \\ \varepsilon_b \\ \varepsilon_c \\ \mathbf{0} \\ \mathbf{0} \end{bmatrix} \\ \mathbf{m}_{ss1} \geq \mathbf{0}, \mathbf{m}_{ds1} \geq \mathbf{0}, \mathbf{m}_{ss2} \geq \mathbf{0}, \mathbf{m}_{ds2} \geq \mathbf{0} \end{cases} \quad (3)$$

where \mathbf{d}_a represents the deformation observed by D-InSAR and GPS caused by Event C, \mathbf{d}_b represents the deformation observed by D-InSAR, SPO and GPS caused by Event D, \mathbf{d}_c is the deformation observed by D-InSAR caused by Events C and D. \mathbf{G}_{ss1} , \mathbf{G}_{ds1} , \mathbf{G}_{ss2} and \mathbf{G}_{ds2} are the Green function matrix of the strike slip and dip slip of Events C and D, respectively. \mathbf{m}_{ss1} , \mathbf{m}_{ds1} , \mathbf{m}_{ss2} and \mathbf{m}_{ds2} represent the matrix of strike slip and dip slip of these two events, respectively. \mathbf{H}_{ss1} , \mathbf{H}_{ds1} , \mathbf{H}_{ss2} and \mathbf{H}_{ds2} represent the Laplace smoothing constraint matrices of strike slip and dip slip of the two events, respectively. Since the location of the two earthquakes is very close and the underground structures are similar, we used one smoothing factor λ for the joint inversion. Only the high quality InSAR data were chosen for inversion (coherence ≥ 0.9) in Event C to avoid the noise.

3. Results

The results of coseismic deformation and source parameters of the four events are shown in Figs. 3, 4, 5 and Table 2. As these figures shown, these four earthquakes caused subsidence that accompanied

Table 2

The source parameters of Event A–D.

Earthquake	Length (km)	Strike (°)	Dip (°)	Average rake (°)	Mo 10 ¹⁸ Nm	M_w
Event A	30	119–151	46.8	–105.1	2.71	6.26
Event B	34	131–177	44.9	–75.0	2.26	6.20
Event C	40	128–175	33.5	–67.4	2.15	6.19
Event D	40	128–175	33.5	–64.1	9.14	6.60

Note. Events C and D occurred in the northern and southern segments of the same fault.

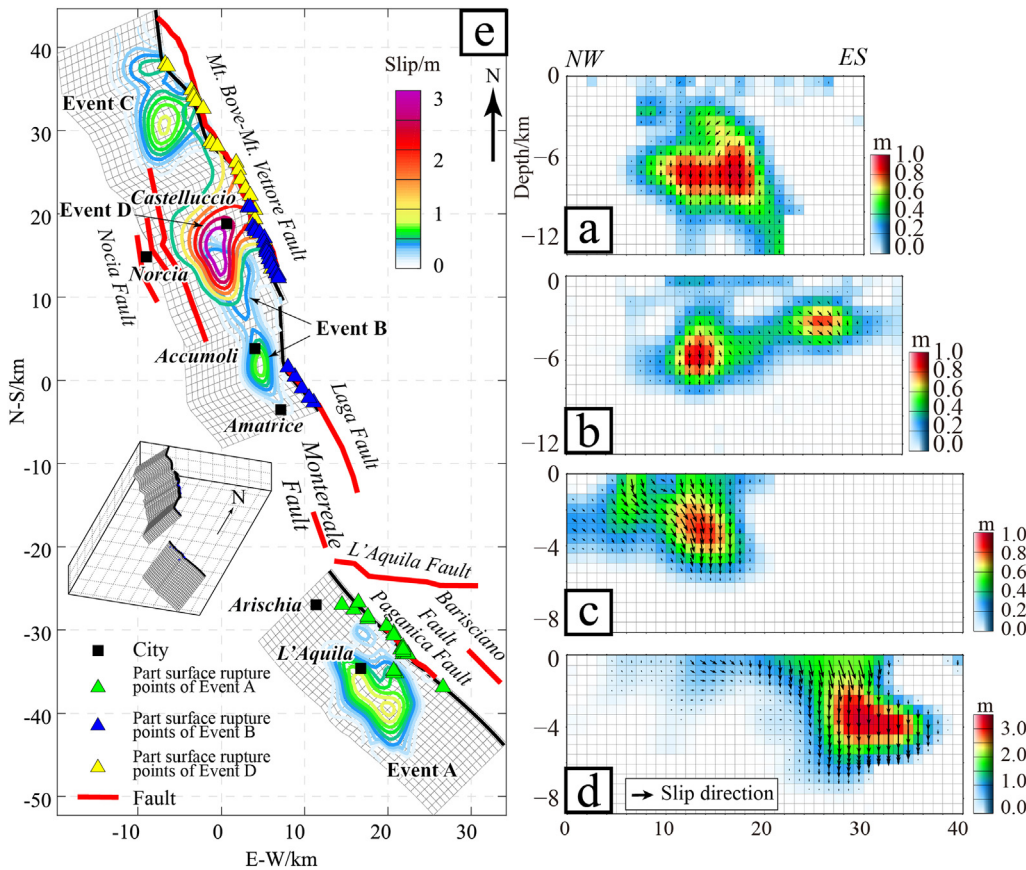


Fig. 2. Slip distribution models of (a) Event A, (b) Event B, (c) Event C and (d) Event D. (e) The location distribution of the models and the part of surface rupture points caused by these four earthquakes (Michetti et al., 2000; EMERGEO, 2010; Piccardi et al., 2016; Civico et al., 2018; Villani et al., 2018).

with some horizontal deformations. The InSAR results are consistent with the GPS observations, with the average root mean square (RMS) of 3.7 mm, 3.0 mm, 2.1 mm and 2.4 mm for Events A, B, C and D, respectively. The slip distribution models of the four earthquakes are shown in Fig. 2.

3.1. Event A: the Apr. 6th, 2009 earthquake

The coseismic deformation fields of Event A are shown in Fig. 3a, d and g. The maximum LOS deformations of ascending ALOS, ascending and descending Envisat are 19.5 cm, 20.6 cm and 25.4 cm, respectively.

We constructed variable-strike fault models for Events A, B, C, and D (Fig. 2a, b, c and d), which have a higher accuracy than the consistent-strike fault model, thereby improve the inversion accuracy. The slip distribution of Event A shown in Fig. 2a indicates that it is a normal slip with some right-lateral components, and the main fracture is located at 2 to 10 km depth. The maximum normal slip is 0.94 m at 8 km depth. The moment tensor magnitude is 2.71×10^{18} Nm, corresponding to M_w 6.26. Using the slip distribution model (Fig. 2a), we simulated the corresponding deformation field of InSAR and GPS (Fig. 3). The results are in agreement with the results of other studies (Atzori et al., 2009; Walters et al., 2009; De Natale et al., 2011).

3.2. Event B: the Aug. 24th, 2016 earthquake

The deformation of Event B, shown in Fig. 4a and d, is similar to that of Event A. The deformation fields show an NNW-SSE strike along Mt. Laga and Mt. Vettore. Both the ascending and descending images show two major subsidence areas. Combing the ascending and descending Sentinel-1(S1) data, we obtained two deformation components (east-west and vertical) with the assumption that there is no north-

south deformation in Fig. S4. The maximum vertical deformation is 20.3 cm in the northwest of the epicenter (marked by arrow 1 in Figs. 4a and S4a).

As Fig. 2b shows, the slip characteristics are consistent with the surface deformation, and there are also two asperities at 6 km (asperity 1) and 3 km (asperity 2) depth. The major slip is a dip-slip of a normal fault, concentrating at 2–8 km depth. The maximum slip 0.92 m is inverted at asperity 1 (Fig. 4a). The final moment tensor of Event B is 2.26×10^{18} Nm, corresponding to M_w 6.20, and the fitting RMS of ascending and descending images are 1.46 cm and 1.50 cm. The result agrees with that of Cheloni et al. (2017), USGS (2018) and GCMT (2018).

The estimated results obtained by the fault model of Event B (Fig. 4b and e) are consistent with the real observations. The fitting residuals of GPS horizontal and vertical deformation are 0.16 cm and 0.39 cm, respectively.

3.3. Events C/D: the Oct. 26th and Oct. 30th, 2016 earthquakes

The coseismic deformation fields of Events C and D are hard to distinguish because they occurred only 4 days apart (Table S1). Fortunately, the independent coseismic deformation fields of Event C and Event D were obtained by 3 ascending SAR images shown in Fig. 5a and d. Event C has serious phase decorrelation and noise and its maximum LOS deformation is up to 17.4 cm. Event D is the largest earthquake among the four events. It caused great surface deformations (Civico et al., 2018; Villani et al., 2018), filling the earthquake gap between Events B and C (Stein and Sevilgen, 2016; Mildon et al., 2017).

In Fig. 5j, although the deformation of the ascending image is affected by Event D, the deformation information on the north of the epicenter of Event C is well preserved. Compared with the ascending

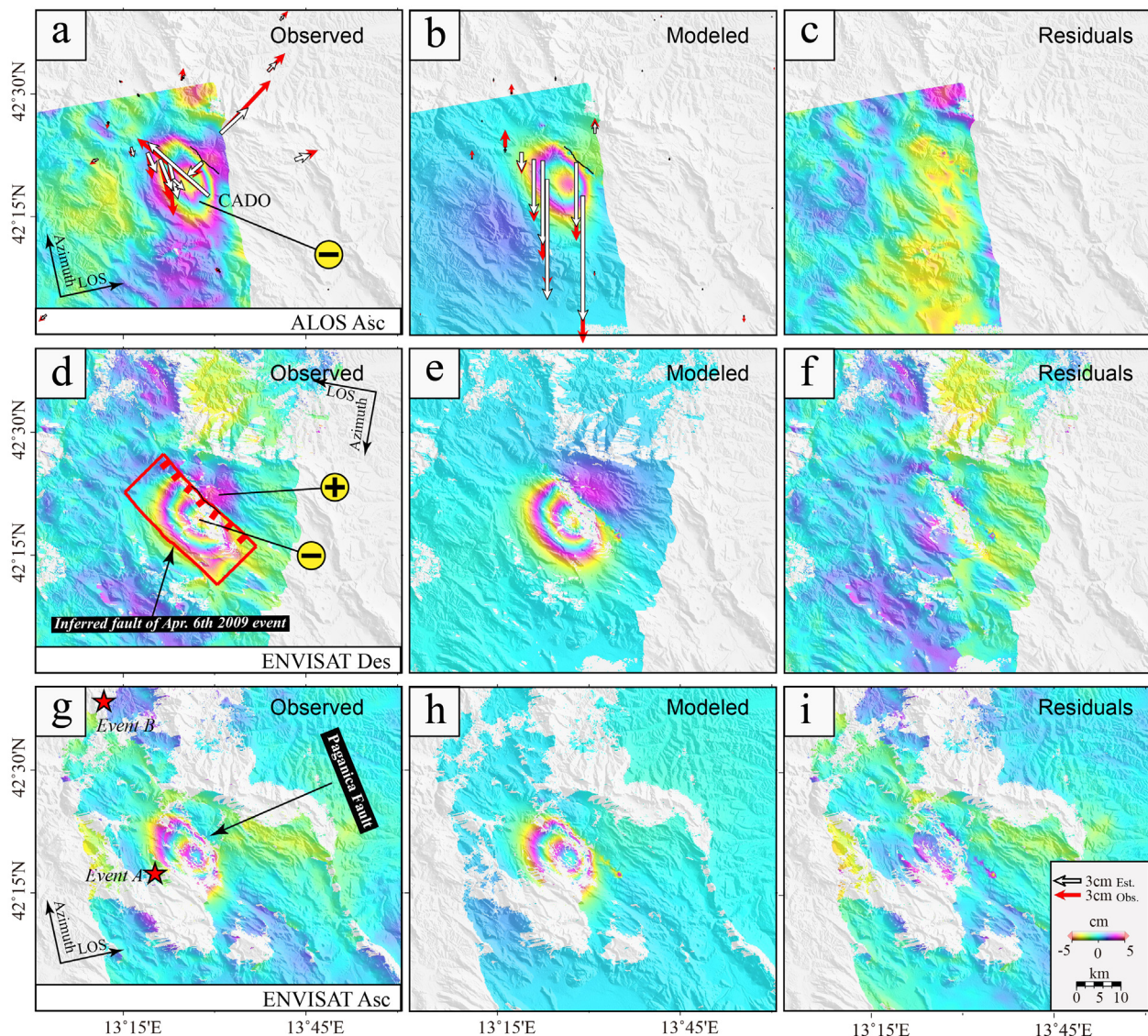


Fig. 3. Geodetic displacement fields for Event A. Observed, estimated displacements, and residuals of the ascending ALOS image (panels a, b and c), descending ENVISAT image (d, e, f) and ascending ENVISAT image (g, h, i). The observed (red arrow) and estimated (white arrow) horizontal and vertical GPS displacements are shown in panels (a) and (b). (For interpretation of the references to colour in this figure legend, the reader is referred to the web version of this article.)

images (Fig. 5d and j), the descending image (Fig. 5g) provides more information of the area on the west of the epicenter of Event C and on the east of the epicenter of Event D. The differences between the ascending and descending images indicate that Event D not only caused large vertical deformations but also led to some horizontal deformations (Fig. 5g and j). Because of the horizontal deformations, satellites observing from opposite directions obtained opposite phases on the west of the epicenter of Event D.

The slips of Event C are concentrated in the 0–5 km range below the surface with the maximum value of 0.84 m located at ~4 km depth, as shown in Fig. 2c. Similar to Event B, the fault of Event C is also a normal fault dominated by dip slips and accompanied with some left-lateral strike slips. All these slip distributions extended to the ground surface, and caused serious incoherence in InSAR images. The slip model of Event D is shown in Fig. 2d. Most slips are located at 0–6 km depth and the maximum slip is 3.44 m. The normal fault with some left-lateral gradually changed to a pure normal fault downward. The fracture close to the surface caused large intensive surface ruptures. This also explains why the InSAR observations of the epicentral region are almost incoherent. The moment tensor of Events C and D are 2.15×10^{18} Nm

and 9.14×10^{18} Nm, corresponding to M_w 6.19 and M_w 6.60, respectively.

The simulated phases of InSAR are shown in Fig. 5b, e, h, and k. The fitting RMS of Fig. 5a, d, g and j are 0.31 cm, 1.34 cm, 1.92 cm and 3.13 cm, respectively. The estimated results of Event C are shown in Fig. 5b, where the coseismic deformation features of the earthquake are mostly reflected, and the fringes of subsidence area are obvious. The horizontal fitting RMS of GPS (Fig. 5a) are 0.23 cm. However, for the vertical deformation, the observed results are quite different from that obtained by the slip model (fitting RMS is 0.45 cm). This may attribute to the low accuracy of GPS vertical observation and the impacts of aftershocks of Event B. The estimated results of Event D are shown in Fig. 5e, where the simulated phases well restore the observation value near the epicenter, and the fringes on the east and west of the epicenter are clear. The horizontal and vertical observations of GPS are well restored, especially at the VETT station. The fitting RMS of the horizontal and vertical observations are 0.80 cm and 3.88 cm, respectively. The combined slip model of Events C and D is used to obtain the simulated deformations of InSAR observed by ascending and descending data which contain the displacements caused by the two earthquakes. The

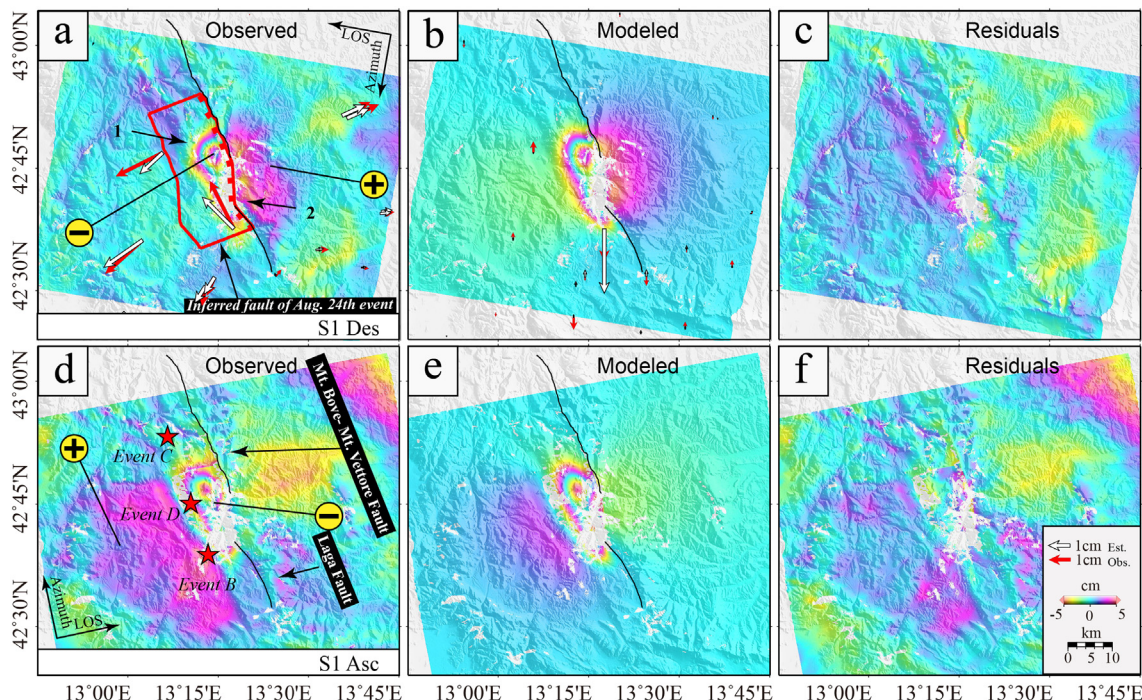


Fig. 4. Geodetic displacement fields for Event B. Observed, estimated displacements, and residuals of the ascending (panels a, b, c) and descending (d, e, f) Sentinel1 image. The observed (red arrow) and estimated (white arrow) horizontal and vertical GPS displacements are shown in panels (a) and (b). (For interpretation of the references to colour in this figure legend, the reader is referred to the web version of this article.)

results are shown in Fig. 5g and j. The joint estimated results basically fit the observations, and the fitting deformation fields of Events C and D are independent and clear.

4. Static Coulomb stress change model

The static Coulomb stress changes on surrounding faults after the main shock is often used to detect the triggering relation between earthquakes (Stein and Lisowski, 1983; Freed, 2005; Console et al., 2008). We combined the dislocation model (Okada, 1992) with the static stress change model (Formula 4) to analyze the triggering mechanism of earthquakes. In this study, the Coulomb 3.3 code developed by USGS (Lin and Stein, 2004; Toda et al., 2005, 2011) was used to obtain the Coulomb stress change. The stress change model is as follows:

$$\Delta\text{CFS} = \Delta\tau + \mu'\Delta\sigma_n \quad (4)$$

where ΔCFS represents the Coulomb stress change of the receiving fault, $\Delta\tau$ is the change value of shear force along the fault slip, μ' represents the effective friction coefficient, and $\Delta\sigma_n$ is the change of the positive stress on the receiving fault plane (take tensile stress as the positive). The Young's modulus, Poisson factor and effective friction coefficient are set to 8×10^{15} Pa, 0.25 and 0.4 respectively.

Firstly, we successively calculated the cumulative impact of previous earthquakes on the receiving faults (Fig. 6). The parameters of the causative fault and the receiving fault adopted the fault geometries and slip parameters obtained above. The causative faults of the three latter earthquakes all show stress increasing after Event A. As shown in Fig. 6a, the epicenters of Events B, C and D are located in the region with positive stress changes caused by Event A. However, because of the long distance between them and Event A, the increments of Coulomb stress are not significant, with the maximum value of 0.01 MPa. The epicenter of Event B is located in the region with great stress growth, indicating that Event A might have accelerated the occurrence of Event B. As shown in Fig. 6b, Events A and B have a great effect on the causative faults of Events C and D. The stress changes on the

causative fault of Events C and D are mostly positive, with the maximum value of 2.48 MPa. On the causative region of Event C (north segment), the average Coulomb stress increased by 0.15 MPa. On the causative region of Event D (south segment), the stress changes (both positive and negative) caused by the former three earthquakes together are larger than 0.1 MPa (Fig. 6c). The stress reduction sections are in the slip regions of the causative fault of Event B, which means the stress in this region was released during Event B. The surrounding regions, without slip, have a larger stress increment due to the combined action of the former three earthquakes.

Moreover, we calculated the cumulative stress changes on the surrounding faults after these four earthquakes. We have collected the fault parameters of the major faults in the area (Blumetti, 1995; Michetti et al., 2000; Boncio et al., 2004; Basili et al., 2008; Di Bucci et al., 2011). And the width of faults has been extended to 20 km so that we can observe the changes at the bottom of the fault, though the actual fault may not be so deep. In order to obtain finer results of stress change, each fault is sub-divided into patches of $2 \text{ km} \times 2 \text{ km}$. Using the Coulomb 3.3 software (Toda et al., 2011), we obtained the final result as shown in Fig. 7. The stress changes of the causative fault are basically negative, which means the energy in these regions were released. And an earthquake gap (black dashed rectangle in the center of Fig. 7) has been identified between Events A and B. This gap is in the southern segment of the big gap between Event A and the 1997 Umbria-Marche M_w 6.0 event (the northern segment has been filled by Events B, C and D) (Mildon et al., 2017). There is absence of earthquake in the unfilled gap since 1859. Some scholars believe that the gap may have the risk of an $\sim M$ 6 earthquake (Stein and Sevilgen, 2016).

Due to the combined action of the four earthquakes the Coulomb stress, on the Montereale fault, the average Coulomb stress increased by 0.05 MPa, and the maximum increment of 0.08 MPa. Several faults in the southeast of L'Aquila also have Coulomb stress increase, such as the Barisciano fault and Castel di Ieri fault. The Barisciano fault has the greatest Coulomb stress increase (average 0.06 MPa, maximum 0.22 MPa), as it is closer to the Paganica fault.

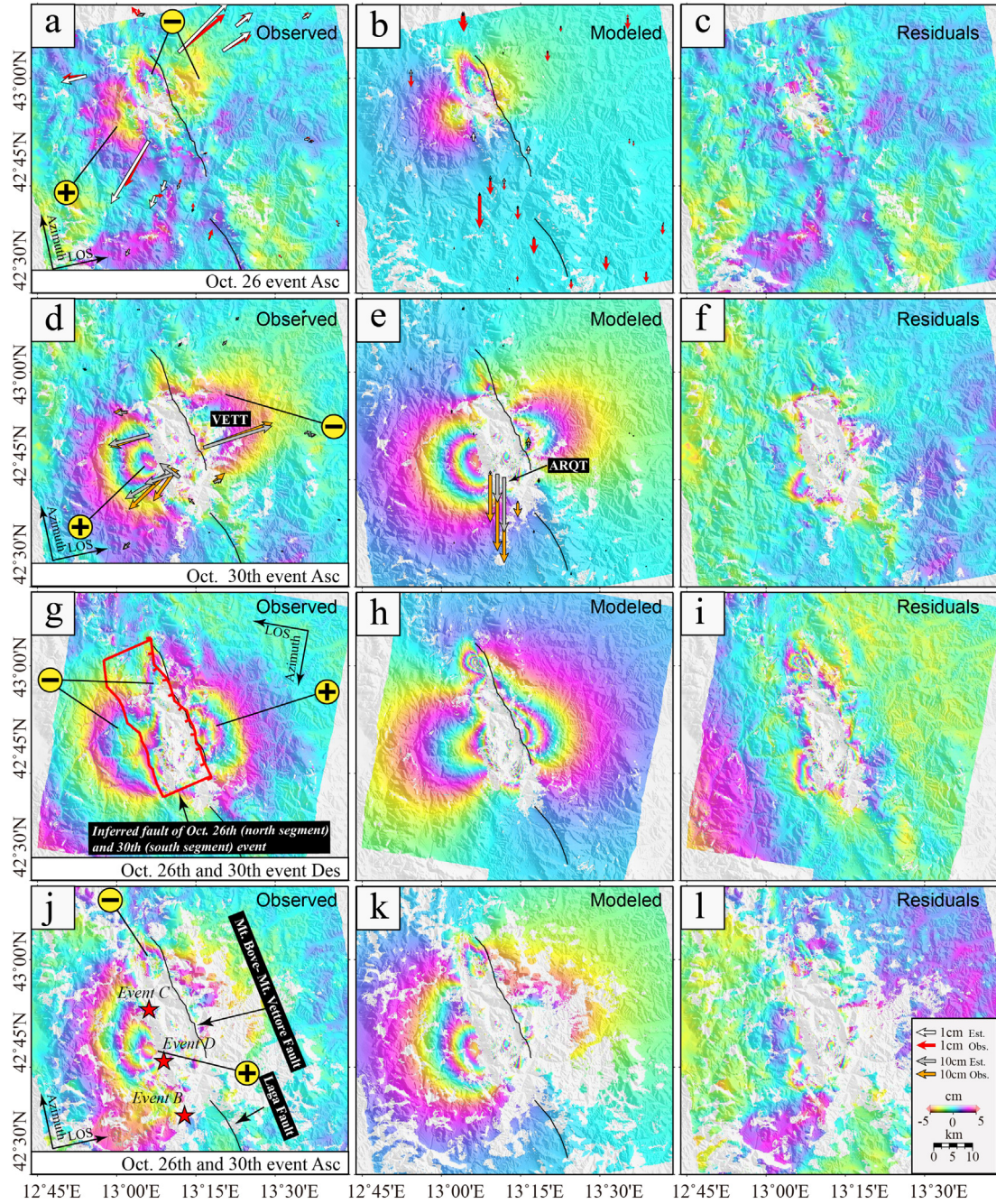


Fig. 5. Geodetic displacement fields for Events C and D. Observed (a, d, g, j) and estimated (b, e, h, k) deformations, and residuals (c, f, i, l) of descending and ascending Sentinel-1A/B tracks interferograms caused by Events C and D. The arrows show observed (red and yellow) and estimated (white and gray) horizontal (a, b) and vertical (d, e) GPS displacements caused by Events C and D. (For interpretation of the references to colour in this figure legend, the reader is referred to the web version of this article.)

5. Discussion and analysis

5.1. Rupture features

All slip distribution models (Fig. 2) show that each causative fault of the four events has an obvious fault slip near the surface, indicating that these earthquakes caused different degrees of surface ruptures. The slips zones obtained by the models coincide with the surface rupture points of Events A and B obtained by the field work (EMERGE, 2010, 2016a,b). The four earthquakes are all mainly caused by normal slips. Events A and B have little strike-slip components. However, Events C and D have more left-lateral strike-slip components on the causative

faults. The average strike-slip of Event C is 0.04 m, accounting for about 35% of the total slip. Event D caused a large left-lateral strike-slip 0–2 km below the surface. The average strike-slip is 0.05 m with the maximum value of 0.71 m, accounting for about 12% of the total slip. The rake angle is different from -80 to -90° given by USGS (2018), GCMT (2018) or INGV (2018). But it is in line with the phenomenon in the Fig. 5g and j that the deformations on the west of the epicenter of the ascending and descending track images are opposite. Some strike-slip components can also be seen in the results of Cheloni et al. (2017). So, the results of the relevant agencies and other researches (Xu et al., 2017) might underestimate the strike-slip component.

Our results show that, in Event B, the maximum slip is 0.92 m. Using

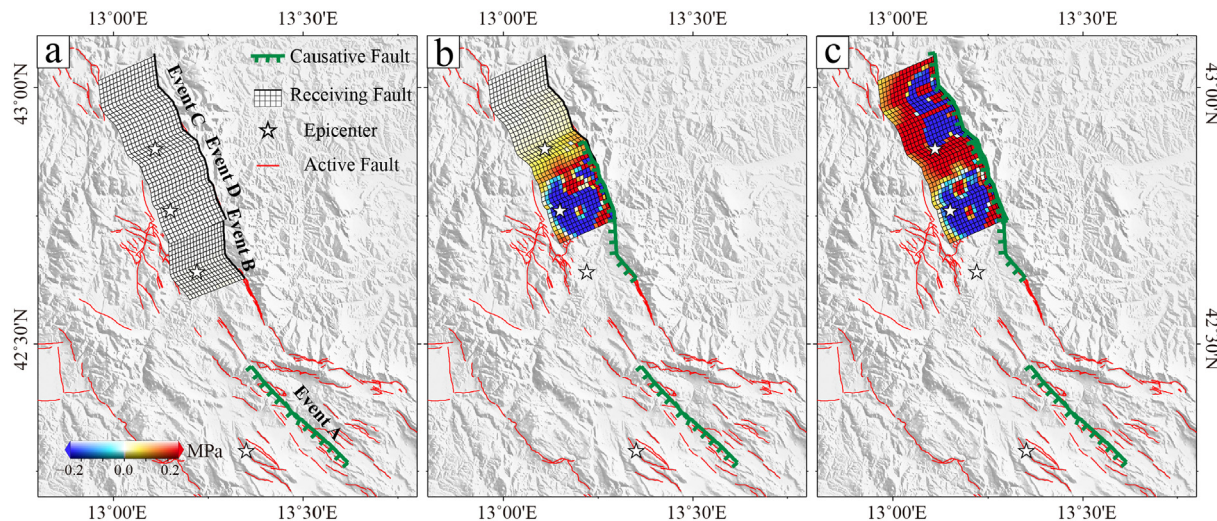


Fig. 6. Coulomb stress changes associated with Events A, B, C and D. (a) The Coulomb stress changes on the causative faults of Events B, C and D caused by Event A; (b) the cumulative Coulomb stress from Events A and B; (c) the cumulative Coulomb stress from Events A, B and C.

the seismic wave data, Tinti et al. (2016) and Magnoni and Casarotti (2016) inversed the slip distributions of Event B and got the maximum slip ~ 1 m located at asperity 2. Cirella and Piatanesi (2016), Huang et al. (2017) and Cheloni et al. (2017) reported that the maximum slip (~ 1.5 m) is located at asperity 1 (Fig. 2b). It should be noted that Huang et al. (2017) and Cheloni et al. (2017) adopted a double-fault model, but other studies adopted the fault model with a consistent-strike. Our study adopts a variable-strike fault geometry when inverting the slip distribution, which is a marked difference between our study and previous publications. We have made a comparative experiment on the consistent-strike model and variable-strike model. The results show that the fitting accuracy of ascending and descending images of Event B

are increased by 2.8% and 25%, respectively. Because the fault dips in this region are similar (Boncio et al., 2004), our variable-strike model can well reflect their slip no matter Event B is caused by one or two faults. In fact, as fault slip distribution in Fig. 2b and e shows, there is still a certain fault slip on the north side of the Laga fault, which has not extend to the south side of the Laga fault. So we think that the actual slip regions are the Mt. Bove - Mt. Vettore fault and the north segment of the Laga fault.

The slip distribution of Event C we got are similar to those of Cheloni et al. (2017) obtained from different SAR data, but the maximum slip and the moment tensor are different. It is due to the different data sources and fault models. Based on the analysis of the historical

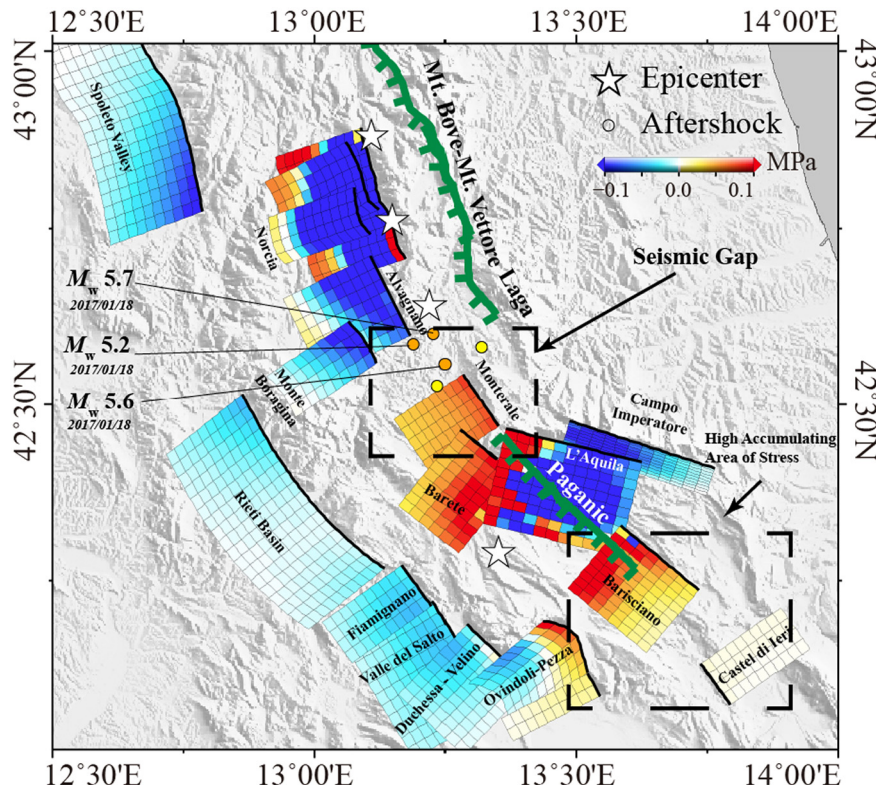


Fig. 7. The Coulomb stress changes on neighboring faults caused by Events A, B, C and D jointly. The data of neighboring faults are from the ITHACA database (Michetti et al., 2000), DISS database (Basilì et al., 2008) and other related literature (Blumetti, 1995; Di Bucci et al., 2011; Boncio et al., 2004).

data, the field work data, and SAR observations, we adopted three fault models of variable strike for Events A, B, C and D, because the consistent-strike model increases the inversion error near the surface. Cheloni et al. (2017) adopted two single-strike fault models for Events C and D. In addition, the SAR data they used contain the deformation caused by several events, which may result in underestimation of the deformations and energy released by Event C. For Event D, both the GPS data inversion results of INGV working group (INGV, 2016) and our results show the slips are spread to the surface. However, the surface slips retrieved by the seismic data from INGV working group are too small (< 1 m), which conflicts the surface rupture data provided by Villani et al. (2018) (many observation slips > 1.5 m with the maximum slip ~ 2.5 m). Same as Events A and B, we adopted one variable-strike model for Events C and D. The results of comparative experiments show that in addition to a 17.6% reduced of fitting accuracy of descending image, the ascending images of Events C, D and containing both Events C and D are increased by 11.3%, 66.0% and 55.0%, respectively. And the strike angle of the fault is also more in line with the actual rupture (Figs. 2e, S5).

5.2. The triggering relationships among causative faults

The causative faults of Events B, C and D are all located in regions with positive Coulomb stress changes caused by Event A, especially the Laga fault, near the epicenter of Event A, which is one of the causative faults of Event B. The maximum stress increment in the Laga fault is 0.01 MPa. This means Event A might have accelerated the occurrence of the latter earthquakes on these faults. However, the stress increment of these faults are generally small, which cannot rules out the possibility that the latter three earthquakes and Event A are independent events.

After Event B, the causative fault of Events C and D experienced an increase in average Coulomb stress of 0.78 MPa, with the maximum increment of over 2.48 MPa except for the slip area. The epicenter of Event C is in the area with stress increment. Then, we calculated the stress effects of the first three earthquakes on the causative fault of Event D. Unlike the previous earthquakes, the epicenter of Event D is located in the region with stress reduction, and the hypocenter position coincides with the main slip region of Event B. Moreover, a slip area of Event D overlapped the main slip region of Event B. These indicate that Events D and B were likely caused by the slip of the same fault. The energy of the Mt. Vettore fault was not fully released in Event B, so the fault was unstable. The occurrence of Event C again triggered the fault slip and led to the occurrence of Event D.

Through the above analysis, we can make the following speculations: Event A increased the stress the NW and SE of its epicenter and accelerated the energy accumulation of the Laga fault and Vettore fault, but there is no obvious triggering relationship between Event A and subsequent earthquakes. After Event A, these faults of positive stress kept accumulating energy for 7 years, which finally led to the occurrence of the Aug. 24th, 2016 M_w 6.3 earthquake (Event B).

5.3. Impacts on surrounding faults and seismic risk assessment

As can be seen from Figs. 6 and 7, there is a seismic gap between the seismogenic zone of Events A and B. Moreover, the region has experienced positive Coulomb stress changes from Event A to Event D. In this gap, the Montereale fault has the most significant stress increase. In 1703, an M 6.7 earthquake occurred on the fault caused surface ruptures of different degrees in the west of the Mt. Laghetto Ridge and Montereale basin (Blumetti, 1995). The slip rate of the fault is 0.1–1 mm/yr (Basili et al., 2008). If we take the middle rate of 0.5 mm/yr, the Montereale fault area has accumulated about 1.01×10^{18} Nm since 1703, which equivalent to the energy of an M_w 6.0 earthquake, though several small earthquakes (about M_w 5.0) (USGS, 2018; INGV, 2018) have occurred during the period. In 2017, three $M_w > 5$ aftershocks occurred around the south Laga fault within the region of the

seismic gap (Fig. 7) (Mildon et al., 2017; INGV, 2017) which confirmed our results (Fig. 7). But these small aftershocks only released a small amount of energy, so a large amount of accumulated energy remains locked. And we believe that the region has a great risk of earthquake in the future. In addition, although the three $M_w > 6$ earthquakes in 2016 gradually filled up the gap (except the region of the black dashed rectangle in the center of Fig. 7) between the 1997 Umbria-Marche M_w 6.0 event and Event A, the south side of Event A is still in the principal axial region with large strain rate (D'Agostino et al., 2009). Meanwhile, the Coulomb stress increased in this region has been increasing since Event A. The largest increment is in the Barisciano fault, which reaches to 0.22 MPa. The region accommodated many earthquakes of M 4–5 in the history (Di Bucci et al., 2011). However, as the accumulated stress has not been fully released, the region has a great risk of earthquake in the future. This region deserves our continuous attention and in-depth study.

There are many normal faults in the extension area. The earthquake series in central Italy provides an opportunity to study the mechanism and triggering relationship of the earthquake sequence caused by normal faults. The fault system and movement characteristics in central Italy are similar to the northern Ethiopian rift (Keir et al., 2006). They are located in the transition area of blocks and are dominated by normal faults. However, the earthquakes occurred in the latter region are not great (most of them less than M_w 6.0) (USGS, 2018). This may be related to the existence of volcanoes there. The fluid under the volcanoes may obstruct fault rupture, making it difficult to accumulate energy and produce a series large earthquakes such as this central Italy earthquake sequence (Lin et al., 2016).

6. Conclusion

In this research, three variable-strike fault models of the four earthquakes in central Italy (Events A/B/C/D) were retrieved with multiple datasets of coseismic deformations from InSAR and GPS. We also analyzed the effects of Coulomb stress changes between these earthquakes and on the surrounding faults.

From the above work, we draw the following conclusions:

1. These four earthquakes all occurred in the Apennine Mountains region and have very similar focal mechanism solutions, which confirm that the central Apennine Mountains are dominated by a normal faulting.
2. The fault model with variable-strike can be more consistent with the actual fault strike and improve the overall fitting precision.
3. The slips of Events C and D are not nearly pure normal slips, as reported by USGS (2018), GCMT (2018) and Xu et al. (2017), but strike slips with left-lateral components.
4. The results of Coulomb stress changes among the four earthquakes indicate that Event A may have accelerated the occurrence of Event B and, after Event B, the maximum stress increment of over 2.48 MPa have been found in the causative faults of Events C and D which is above the empirically triggering threshold 0.01 MPa (Lorenzo-Martín et al., 2006).
5. There was a seismic gap between Event A and Event B. Moreover, the Montereale fault has a period free of strong earthquakes longer than 300 years since the 1703 M 6.7 earthquake, so it has a great risk of earthquake in the future. In addition, the Barisciano fault located in the southeast of the Paganica fault also has a large risk of earthquakes.

Acknowledgments

We thank the anonymous reviewer for his/her careful reading and precious suggestions. This work was supported by the National Natural Science Foundation of China (41664001), Support Program for Outstanding Youth Talents in Jiangxi Province (20162BCB23050) and

Sheng Hua Yu Ying plan of Central South University (502034003). The SAR data of Sentinel-1, Envisat and ALOS are obtained from the scientific data center of ESA (European Space Agency, 2009, 2018). Original ALOS data are copyright by Japan Aerospace Exploration Agency (JAXA). Some of the images in this study were drawn using the Generic Mapping Tools (GMT) which is an open source software.

Appendix A. Supplementary data

Supplementary data to this article can be found online at <https://doi.org/10.1016/j.tecto.2018.07.013>.

References

- Atzori, S., Hunstad, I., Chini, M., Salvi, S., Tolomei, C., Bignami, C., Stramondo, S., Trasatti, E., Antonioli, A., Boschi, E., 2009. Finite fault inversion of DInSAR coseismic displacement of the 2009 L'Aquila earthquake (central Italy). *Geophys. Res. Lett.* 36 (15). <https://doi.org/10.1029/2009GL039293>.
- Basili, R., Valensise, G., Vannoli, P., Burrato, P., Fracassi, U., Mariano, S., ... Boschi, E., 2008. The Database of Individual Seismogenic Sources (DISS), version 3: summarizing 20 years of research on Italy's earthquake geology. *Tectonophysics* 453 (1–4), 20–43. <https://doi.org/10.1016/j.tecto.2007.04.014>.
- Blumetti, A.M., 1995. Neotectonic investigations and evidence of paleoseismicity in the epicentral area of the January–February 1703, Central Italy, earthquakes. *Perspect. Paleoseismol.* 6, 83–100.
- Boncio, P., Lavecchia, G., Pace, B., 2004. Defining a model of 3D seismogenic sources for Seismic Hazard Assessment applications: the case of central Apennines (Italy). *J. Seismol.* 8 (3), 407–425.
- Cheloni, D., De Novellis, V., Albano, M., Antonioli, A., Anzidei, M., Atzori, S., Avallone, A., Bignami, C., Bonano, M., Calcaterra, S., Castaldo, R., Casu, F., Cecere, G., De Luca, C., Devoti, R., Di Bucci, D., Esposito, A., Galvani, A., Gambino, P., Giuliani, R., Lanari, R., Manunta, M., Manzo, M., Mattone, M., Montuori, A., Pepe, A., Pepe, S., Pezzo, G., Pietranonio, G., Polcaro, M., Riguetti, F., Salvi, S., Sepe, V., Serpelloni, E., Solaro, G., Stramondo, S., Tizzani, P., Tolomei, C., Trasatti, E., Valerio, E., Zinno, I., Doglioni, C., 2017. Geodetic model of the 2016 Central Italy earthquake sequence inferred from InSAR and GPS data. *Geophys. Res. Lett.* 44, 6778–6787. <https://doi.org/10.1002/2017GL073580>.
- Cirella, A., Piatanesi, A., 2016. Source Complexity of the 2016 Amatrice Earthquake from Non Linear Inversion of Strong Motion Data: Preliminary Results, Zenodo. Available from: <https://doi.org/10.5281/zenodo.153821> Accessed March 2018.
- Cirella, A., Piatanesi, A., Cocco, M., Tinti, E., Scognamiglio, L., Michelin, A., Lomax, A., Boschi, E., 2009. Rupture history of the 2009 L'Aquila (Italy) earthquake from non-linear joint inversion of strong motion and GPS data. *Geophys. Res. Lett.* 36 (19). <https://doi.org/10.1029/2009GL039795>.
- Civico, R., Pucci, S., Villani, F., Pizzimenti, L., De Martini, P.M., Nappi, R., Open MERGEO Working Group, 2018. Surface ruptures following the 30 October 2016 M w 6.5 Norcia earthquake, central Italy. *J. Maps* 14 (2), 151–160. <https://doi.org/10.1080/17445647.2018.1441756>.
- Console, R., Murru, M., Falcone, G., Catalli, F., 2008. Stress interaction effect on the occurrence probability of characteristic earthquakes in Central Apennines. *J. Geophys. Res. Solid Earth* 113 (B8). <https://doi.org/10.1029/2007JB005418>.
- D'Agostino, N., Mantenuto, S., D'Anastasio, E., Avallone, A., Barchi, M.R., Collettini, C., Radicioni, F., Stoppini, A., Fastellini, G., 2009. Contemporary crustal extension in the Umbria-Marche Apennines from regional CGPS networks and comparison between geodetic and seismic deformation. *Tectonophysics* 476, 3–12. <https://doi.org/10.1016/j.tecto.2008.09.033>.
- De Natale, G., Crippa, B., Troise, C., Pingue, F., 2011. Abruzzo, Italy, earthquakes of April 2009: heterogeneous fault-slip models and stress transfer from accurate inversion of ENVISAT-InSAR data. *Bull. Seismol. Soc. Am.* 101 (5), 2340–2354. <https://doi.org/10.1785/0120100220>.
- Di Bucci, D., Vannoli, P., Burrato, P., Fracassi, U., Valensise, G., 2011. Insights from the Mw 6.3, 2009 L'Aquila earthquake (Central Apennines)—unveiling new seismogenic sources through their surface signatures: the adjacent San Pio Fault. *Terra Nova* 23 (2), 108–115. <https://doi.org/10.1111/j.1365-3121.2011.00990.x>.
- EMERGEO, W.G., 2010. Evidence for surface rupture associated with the Mw 6.3 L'Aquila earthquake sequence of April 2009 (central Italy). *Terra Nova* 22 (1), 43–51. <https://doi.org/10.1111/j.1365-3121.2009.00915.x>.
- EMERGEO, W.G., 2016a. Coseismic effects of the 2016 Amatrice seismic sequence: first geological results. *Ann. Geophys.* 59 [\(Fast Track 5\)](https://doi.org/10.4401/ag-7195).
- EMERGEO, W.G., 2016b. Surface ruptures associated with the Mw 6.1 L'Aquila earthquake sequence of April 2009 (Central Italy). Available from: <http://emergeo.ingv.it/pubblicazioni-e-presentazioni.html>, Accessed date: March 2018.
- European Space Agency, 2009. Dataset of SAR products (Envisat and ERS) corresponding to the earthquake of Aquila (Italy). Available from: <https://earth.esa.int/web/guest/data-access/sample-data>, Accessed date: March 2018.
- European Space Agency, 2018. Copernicus open access hub. Available from: <https://scihub.copernicus.eu/>, Accessed date: March 2018.
- Faure, W.J.P., Roberts, G.P., Sammonds, P.R., Cowie, P.A., 2010. Comparison of earthquake strains over 10° {2} and 10° {4} year timescales: insights into variability in the seismic cycle in the central Apennines, Italy. *J. Geophys. Res.* 115 (B10), B10418.
- <https://doi.org/10.1029/2009JB006462>.
- Feng, G.C., Li, Z.W., Shan, X.J., Xu, B., Du, Y.N., 2015a. Source parameters of the 2014 Mw 6.1 South Napa earthquake estimated from the Sentinel 1A, COSMO-SkyMed and GPS data. *Tectonophysics* 655, 139–146. <https://doi.org/10.1016/j.tecto.2015.05.018>.
- Feng, G.C., Li, Z.W., Shan, X.J., Zhang, L., Zhang, G.H., Zhu, J.J., 2015b. Geodetic model of the April 25, 2015 Mw 7.8 Gorkha Nepal earthquake and Mw 7.3 aftershock estimated from InSAR and GPS data. *Geophys. J. Int.* 203 (2), 896–900. <https://doi.org/10.1093/gji/ggv335>.
- Freed, A.M., 2005. Earthquake triggering by static, dynamic, and postseismic stress transfer. *Annu. Rev. Earth Planet. Sci.* 33, 335–367. <https://doi.org/10.1146/annurev.earth.33.092203.122505>.
- GCMT, 2018. The global Centroid-Moment-Tensor (CMT) project. Available from: <http://www.globalcmt.org>, Accessed date: March 2018.
- Huang, M.H., Fielding, E.J., Liang, C., Milillo, P., Bekkaert, D., Dreger, D., Salzer, J., 2017. Coseismic deformation and triggered landslides of the 2016 Mw 6.2 Amatrice earthquake in Italy. *Geophys. Res. Lett.* 44 (3), 1266–1274. <https://doi.org/10.1002/2016GL071687>.
- Hunstad, I., Selvaggi, G., D'Agostino, N., England, P., Clarke, P., Pierozzi, M., 2003. Geodetic strain in peninsular Italy between 1875 and 2001. *Geophys. Res. Lett.* 30 (4), 1–4. <https://doi.org/10.1029/2002GL016447>.
- INGV, 2016. Summary report on the October 30, 2016 earthquake in central Italy Mw 6.5, Zenodo. Available from: <https://doi.org/10.5281/zenodo.166238>, Accessed date: March 2018.
- INGV, 2017. Aggiornamento eventi sismici in Italia centrale, 18 gennaio 2017 ore 17:00. Available from: <https://ingvterremoti.wordpress.com/2017/01/18/aggiornamento-eventi-sismici-in-italia-centrale18-gennaio-2017-ore-1700/>, Accessed date: March 2018.
- INGV, 2018. Database of recent earthquakes released by Istituto Nazionale di Geofisica e Vulcanologia. Available from: <http://cnt.rm.ingv.it/en>, Accessed date: March 2018.
- Jiang, G., Xu, C., Wen, Y., Liu, Y., Yin, Z., Wang, J., 2013. Inversion for coseismic slip distribution of the 2010 M w 6.9 Yushu Earthquake from InSAR data using angular dislocations. *Geophys. J. Int.* 194 (2), 1011–1022. <https://doi.org/10.1093/gji/ggt141>.
- Jónsson, S., Zebker, H., Segall, P., Amelung, F., 2002. Fault slip distribution of the 1999 Mw 7.1 Hector Mine, California, earthquake, estimated from satellite radar and GPS measurements. *Bull. Seismol. Soc. Am.* 92 (4), 1377–1389. <https://doi.org/10.1785/0120000922>.
- Keir, D., Ebinger, C.J., Stuart, G.W., Daly, E., Ayele, A., 2006. Strain accommodation by magmatism and faulting as rifting proceeds to breakup: seismicity of the northern Ethiopian rift. *J. Geophys. Res. Solid Earth* 111 (B5). <https://doi.org/10.1029/2005JB003748>.
- Li, H.Y., 2016. Research on Inversion Method for Hypocenter Parameter Base on Dislocation Model. East China University of Technology, Nanchang (Master's thesis) (in Chinese). Retrieved from CNKI. <http://www.cnki.net/>.
- Lin, J., Stein, R.S., 2004. Stress triggering in thrust and subduction earthquakes and stress interaction between the southern San Andreas and nearby thrust and strike-slip faults. *J. Geophys. Res.* 109 (B2). <https://doi.org/10.1029/2003JB002607>.
- Lin, A., Satsukawa, T., Wang, M., Asl, Z.M., Fueta, R., Nakajima, F., 2016. Coseismic rupturing stopped by Aso volcano during the 2016 Mw 7.1 Kumamoto earthquake, Japan. *Science* 354 (6314), 869–874. <https://doi.org/10.1126/science.aah4629>.
- Lorenzo-Martín, F., Roth, F., Wang, R., 2006. Elastic and inelastic triggering of earthquakes in the North Anatolian Fault zone. *Tectonophysics* 424 (3–4), 271–289. <https://doi.org/10.1016/j.tecto.2006.03.046>.
- Magnoni, F., Casarotti, E., 2016. Kinematic finite fault and 3D seismic wave propagation of the 24 August 2016, Mw 6.0 central Italy earthquake. *Ann. Geophys.* 59 [\(Fast Track 5\)](https://doi.org/10.4401/ag-7265).
- Michel, R., Avouac, J.P., Taboury, J., 1999. Measuring ground displacements from SAR amplitude images: application to the Landers earthquake. *Geophys. Res. Lett.* 26 (7), 875–878. <https://doi.org/10.1029/1999GL900138>.
- Michetti, A.M., Serva, L., Vittori, E., 2000. ITIHACA Italy Hazard from Capable Faults: a database of active faults of the Italian onshore territory. In: CD-Rom and Explanatory Notes. ANPA, Rome Available from: <http://sg1.isprambiente.it/geoportal/catalog/main/home.page>, Accessed date: March 2018.
- Mildon, Z.K., Roberts, G.P., Walker, J.P.F., Iezzi, F., 2017. Coulomb stress transfer and fault interaction over millennia on non-planar active normal faults: the Mw 6.5–5.0 seismic sequence of 2016–2017, central Italy. *Geophys. J. Int.* 210 (2). <https://doi.org/10.1093/gji/ggx213>.
- Okada, Y., 1985. Surface deformation due to shear and tensile faults in a half-space. *Bull. Seismol. Soc. Am.* 75 (4), 1135–1154.
- Okada, Y., 1992. Internal deformation due to shear and tensile faults in a half-space. *Bull. Seismol. Soc. Am.* 82 (2), 1018–1040.
- Papadopoulos, G.A., Ganias, A., Agalos, A., Papageorgiou, A., Triantafyllou, I., Kontoes, C., Papoutsis, I., Diakogianni, G., 2017. Earthquake triggering inferred from rupture histories, DInSAR ground deformation and stress-transfer modelling: the case of Central Italy during August 2016–January 2017. *Pure Appl. Geophys.* 174 (10), 3689–3711. <https://doi.org/10.1007/s0024-017-1609-8>.
- Piccardi, L., Blumetti, A.M., Comerci, V., Comerci, V., Di Manna, P., Fumanti, F., Guerrieri, L., Leoni, G., Pompili, R., Vittori, E., Errario, F., Frigerio, C., Livio, F., Michetti, A.M., Bonadeo, L., Brunamonte, F., Sani, F., Tondi, E., Wedmore, L., Roberts, G., Faure-Walker, J., Iezzi, F., Mildon, Z., Gregory, L., Phillips, R., Walters, R., McCaffrey, K., Wilkinson, M., Cowie, P., Rhodes, E., 2016. The August 24, 2016, Amatrice earthquake (Mw 6.0): field evidence of on-fault effects. Retrieved from: http://www.earthquakegeology.com/materials/reports/Amatrice_Earthquake_Report_2016.1.pdf, Accessed date: March 2018.
- Stein, R.S., Lisowski, M., 1983. The 1979 Homestead Valley earthquake sequence,

- California: control of aftershocks and postseismic deformation. *J. Geophys. Res. Solid Earth* 88 (B8), 6477–6490. <https://doi.org/10.1029/JB088iB08p06477>.
- Stein, R., Sevilgen, V., 2016. Italy Earthquake Leaves Seismic Gaps That Were Last Filled by Three Large Earthquakes in 1703. Temblor blog Available from: <http://temblor.net/earthquake-insights/gaps-persist-beyond-ends-m6-2-rieti-italy-earthquake-progressive-sequence-large-shocks-struck-1703-1216/>, Accessed date: March 2018.
- Tinti, E., Scognamiglio, L., Michelini, A., Cocco, M., 2016. Slip heterogeneity and directivity of the ML 6.0, 2016, Amatrice earthquake estimated with rapid finite-fault inversion. *Geophys. Res. Lett.* 43 (20), 10,745–10,752. <https://doi.org/10.1002/2016GL071263>.
- Toda, S., Stein, R.S., Richards-Dinger, K., Bozkurt, S.B., 2005. Forecasting the evolution of seismicity in southern California: animations built on earthquake stress transfer. *J. Geophys. Res.* 110 (B5), B05S16. <https://doi.org/10.1029/2004JB003415>.
- Toda, S., Stein, R.S., Sevilgen, V., Lin, J., 2011. Coulomb 3.3 Graphic-rich deformation and stress-change software for earthquake, tectonic, and volcano research and teaching-user guide. In: U.S. Geological Survey Open-File Report 2011–1060, Available from: <https://pubs.usgs.gov/of/2011/1060/>, Accessed date: March 2018 (63 pp.).
- U. S. Geological Survey (USGS), 2018. Earthquake catalog released by U. S. Geological Survey. Available from: <https://earthquake.usgs.gov/earthquakes/search/>, Accessed date: March 2018.
- Valensise, G., Vannoli, P., Basili, R., Bonini, L., Burrato, P., Carafa, M.M.C., Fracassi, U., Kastelic, V., Maesano, F.E., Tiberti, M.M., Tarabusi, G., 2016. Fossil landscapes and youthful seismogenic sources in the central Apennines: excerpts from the 24 August 2016, Amatrice earthquake and seismic hazard implications. *Ann. Geophys.* 59 <https://doi.org/10.4401/ag-7215>. (Fast Track 5).
- Villani, F., Civico, R., Pucci, S., Pizzimenti, L., Nappi, R., De Martini, P.M., ... Amoroso, S., 2018. A database of the coseismic effects following the 30 October 2016 Norcia earthquake in Central Italy. *Sci. Data* 5, 180049. <https://doi.org/10.1038/sdata.2018.49>.
- Walters, R.J., Elliott, J.R., D'Agostino, N., England, P.C., Hunstad, I., Jackson, J.A., Parsons, B., Phillips, R.J., Roberts, G., 2009. The 2009 L'Aquila earthquake (central Italy): a source mechanism and implications for seismic hazard. *Geophys. Res. Lett.* 36 (17). <https://doi.org/10.1029/2009GL039337>.
- Wang, L.Y., Gao, H., Feng, G.C., 2017. InSAR and GPS inversion for source parameters of the 2016 Mw 6.4 Meinong, Taiwan earthquake. *Chin. J. Geophys.* 60 (7), 2578–2588. <https://doi.org/10.6038/cjg20170707>. (in Chinese).
- Wegmüller, U., Werner, C., 1997. Retrieval of vegetation parameters with SAR interferometry. *IEEE Trans. Geosci. Remote Sens.* 35 (1), 18–24. <https://doi.org/10.1109/36.551930>.
- Xu, G.Y., Xu, C.J., Wen, Y.M., Jiang, G.Y., 2017. Source parameters of the 2016–2017 Central Italy earthquake sequence from the Sentinel-1, ALOS-2 and GPS data. *Remote Sens.* 9 (11), 1182. <https://doi.org/10.3390/rs9111182>.